Superresolution in MRI and its influence in statistical analysis

Pierre Kornprobst, Grégoire Malandain, Olivier Faugeras, R. Peeters, Thierry Viéville, S. Mierisova, S. Sunaert, P. van Hecke

INRIA

INSTITUT NATIONAL DE RECHERCHE EN INFORMATIQUE ET EN AUTOMATIQUE

Superresolution in MRI and its influence in statistical analysis

P. Kornprobst — R. Peeters — T. Vieville — G. Malandain — S. Mierisova — S. Sunaert — O. Faugeras — P. Van Hecke

N° 4513

July 2002

THÈME 3

ISSN 0249-6399 ISRN INRIA/RR--4513--FR+ENG

INRIA
SOPHIA ANTIPOLIS

Superresolution in MRI and its influence in statistical analysis

P. Kornprobst * , R. Peeters † , T. Vieville * , G. Malandain ‡ , S. Mierisova †
, S. Sunaert † , O. Faugeras * , P. Van Hecke †

Thème 3 — Interaction homme-machine,
images, données, connaissances
Projet Odyssée

Rapport de recherche n° 4513 — July 2002 — 36 pages

Abstract: We consider the problem of increasing the spatial resolution of fMRI images. Main contributions are: (1) the definition of the protocol to acquire shifted images in order to be able to obtain images with increased resolution in the slice shift direction; (2) the use of discontinuity preserving regularization methods to solve the problem of superresolution; (3) an evaluation of the results based on human fMRI time series. Activated areas from low, high and superresolved images are compared.

We conclude on the usefulness of using superresolution for task related activation detection.

Key-words: Superresolution, MRI, anisotropic diffusion, half-quadratic minimization

This work was supported by the European project Mapawamo. More information is available on the web site: http://www-sop.inria.fr/epidaure/Collaborations/MAPAWAMO/mapawamo.html

* INRIA Sophia Antipolis, Projet Odyssée
† Department of Radiology, KuLeuven
‡ INRIA Sophia Antipolis, Projet Epidaure

Unité de recherche INRIA Sophia Antipolis
2004, route des Lucioles, BP 93, 06902 Sophia Antipolis Cedex (France)
Téléphone : +33 4 92 38 77 77 —Télécopie : +33 4 92 38 77 65

La super-résolution en IRMf et son influence sur l'analyse statistique

Résumé : Nous étudions le problème de l'augmentation de résolution spatiale pour des images IRMf. Les principales contributions sont: (1) la mise en place d'un protocole expérimental qui permet d'acquérir des images décalées pour obtenir des images de résolution supérieure dans la direction des tranches; (2) l'utilisation de techniques de régularisation avec préservation des discontinuités pour résoudre le problème de la super-résolution; (3) une évaluation des résultats basée sur des séries d'IRMf sur l'homme. Nous comparons les régions activées provenant de l'analyse des séries basse et haute résolution ainsi que reconstruites.

Nous concluons sur l'opportunité d'utiliser une approche de super-résolution pour des taches liées au calcul d'activation.

Mots-clés : Super résolution, IRM, diffusion anisotrope, minimisation semi-quadratique

1 Introduction

Despite the progress in the technology, there is always a demand for proposing methods to improve resolution. Two main reasons account for this need: the cost and the physical limitations of the sensors. A number of applications are concerned like target recognition, surveillance, medical imaging, view synthesis.

Early approaches were based on extrapolating spectrum from a single image [46, 20, 42, 27]. Tsai and Huang [51] first proposed to combine several low resolution images to estimate a high resolution one (see also [44, 1]). Then, most subsequent approaches were based on the constraint that the superresolution image, once warped, blurred and subsampled should give the low resolution images. The differences between the proposed methods come from:

- The modelling of the imaging process which is essential to verify if the estimated solution is consistent with the real data. For instance, in the early contributions [51, 44, 1] the effect of sensor blurring was ignored. More degradations have then been considered like sensor blur [1], noise or motion blur [15, 47, 49, 25, 6]. Another concern is the type of transformation used to correct for the motion blurring between images and how this motion should be estimated. There are again many possibilities like considering affine [26] or projective [35] transformations, non-parametric motion models [45] and region/contour tracking [6]. Finally it is also necessary to consider the subsampling. When the samples from the different low resolution images can be ordered in a regular grid, then the problem becomes very close to image restoration and deconvolution [38]. Notice that this similarity is a source of inspiration for some superresolution algorithms (see for example [12]).

- The prior or constraints imposed on the solution, when the solution isn't unique (because of the image modeling). Priors are usually related to the smoothness of the solution (see for example [7]). However, for high magnification factors, this kind of prior may become ineffective and some recognition based priors can be proposed [5].

- The optimization technique. The direct method consists in minimizing in the least square sense the constraint coming from the image modeling process. Then the problem can be represented as a large sparse linear optimization problem, and solved using explicit iterative methods [12, 7] and preconditioning [36, 38]. Another idea came from Irani and Peleg [26] who introduce the error-backprojection algorithm.

- The domain in which the problem is considered, either spatial or frequency domain [51, 30, 54].

In this paper, we consider the problem of super-resolution from a set of low resolution MRI images with shifts defined by the user of the MR machine. The procedure is described in section 2. It is shown that only shifts in the slice direction may contribute to increase the

[1] Sensor blur which is a result of the convolution of the original signal with the point spread function or the impulse function of the sensor, is an important constraint in any imaging system.

resolution for this specific application. Section 3 sets mathematically the problem and gives different ways to obtain increased resolution images. Simple solutions are first described. They consist in combining the low resolution data. Then, more complex solution are proposed, as solutions of minimization problems involving smoothing terms. This part uses recent developments in nonlinear regularization for image restoration. Section 4 plays an important role in this paper. It shows some results in some synthetic cases but also studies the effects of the different reconstructions with respect to the activation in some human fMRI time series. Section 5 summarizes the paper and draws some conclusions.

2 Multi-aquisitions in MRI

2.1 Problem statement

In functional Magnetic Resonance Imaging (fMRI), a recent application of MRI, the acquired data [55, 33, 40, 41] allows the investigator to visualise brain regions which are responsive to different types of stimuli. Within such an fMRI experiment series of brain images are acquired continuously during different periods of neural activation induced by external inputs or stimuli. The corresponding brain responses induced by these stimuli can be analysed a posteriori with the aid of several different postprocessing packages [53, 19]. This non-invasive technique thus provides neuroscientists with invaluable information to better understand the mechanisms behind the working of the central nervous system.

One of the major goals from the neuroscience point of view is to obtain a spatial resolution in fMRI which allows the investigator to visualise the smallest region of brain activity. In standard fMRI experiments performed on 1.5 Tesla MRI scanners, the typical spatial resolution obtained is about 3×3 mm in plane, with a slice thickness of 3-5 mm, leading to a voxel size of 27-45 mm^3 [48]. To acquire a stack of 32 slices through the entire brain with this resolution using ultra-fast EPI (Echo Planar Imaging) sequences, a time of less than 3 sec is needed. This spatial and temporal resolution is satisfactory in most human studies, but certainly sub-optimal for monkey experiments, given the smaller brain volume of the animal. Even in human experiments a higher spatial resolution would be preferable [39].

Various methods exist to improve the resolution of the fMRI technique. One obvious way to increase the resolution is by reducing the voxel size of the EPI images during acquisition, but this will reduce the signal-to-noise ratio (SNR) considerably [24] (e.g. a decrease of the voxel size by a factor of 2 in all dimensions decreases the SNR of the acquired images by a factor of 8). A possible solution to compensate for this loss of SNR can be to use more averages but the loss in temporal resolution resulting from this adaptation is most of the times unacceptable. A further effect of decreasing the voxel size in the image acquisition protocols is the resulting reduction in volume coverage of the part of the brain which can be scanned within a reasonable temporal resolution and the ensuing problems arising from images fold-over effects in the phase encoding direction.

Another solution to increase the SNR is the use of a higher magnetic field strength. The higher the magnetic field, the higher the induced NMR signal [13, 50]. The disadvantages

of this approach, besides the high cost of high-field NMR scanners, are the potential motion artefacts and the large distortions at brain boundaries which increase with magnetic field strength [14, 29]. Therefore we have considered another approach to increase the resolution of the acquired fMRI datasets, by generating high resolution fMRI images from low resolution fMRI data sets with the aid of newly developed postprocessing techniques. The aim of this study is to demonstrate the applicability of superresolution data postprocessing techniques subsequent to an adapted acquisition scheme to increase the spatial resolution of the calculated functional activation maps, without a significant loss in SNR.

2.2 Aquisition of shifted MRI images

In a standard fMRI experiment an MRI volume is acquired as a stack of 2D images (called image slices) perpendicular to a given direction (slice direction). This is illustrated in Figure 1 (a). The in plane image data are generated by a 2D Fourier Transform of the acquired set of MRI time-domain signals. These time domain signals are encoded with magnetic field gradients in both the x and y direction, applied before and during the acquisition of the signal. These linear field gradients impose a spatial frequency (or phase) dependence on the signal (they relate the resonance frequency of the spins to their spatial position). N time-domain signals encoded with this frequency and phase information are acquired to fill the k-space (dimension N×N). A 2D Fourier transformation of these temporal domain data to the frequency domain results in an MR image consisting of the spatial contrast information of the different tissues in the plane. Hence the name Fourier Transform MRI which is sometimes used for this technique [31, 11].[2]

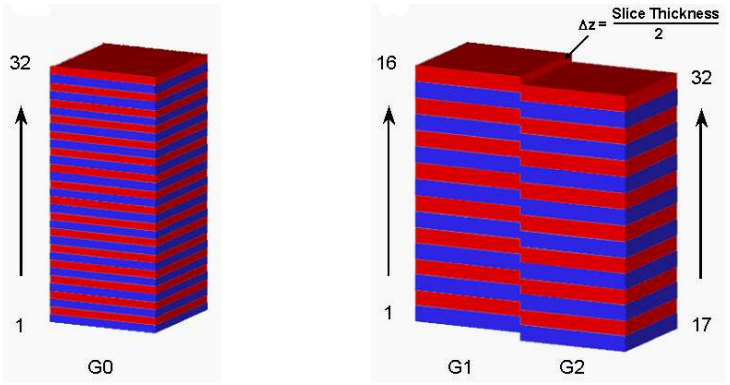

(a) (b)

Figure 1: The acquisition of the different slices in a volume. (a) The slice acquisition sequence in the high resolution dataset (G0). (b) The acquisition sequence in the slice shifted low resolution datasets (G1 and G2).

[2]Other types of MR acquisition protocols are Projection Reconstruction [32] and Spiral MRI.

In MRI, superresolution is only beneficial in the slice direction (perpendicular to the image plane), since shifted slices correspond to different parts of the object in the image space. In plane shifting in the image space, does not add any new information [22], due to the properties of the 2D inverse Fourier Transform used in MR imaging. Thus in plane shifting in the image space, is nothing else than a global phase shift in the acquisition space, the original temporal domain, which does not affect the inherent spatial frequency resolution of the acquired data.

In practice we will acquire only images shifted in the slice direction. In order to obtain two different sets of shifted volumes, the fMRI acquisition protocol has to be adapted. The two different volumes will be acquired in an interleaved fashion where the first volume is positioned with a relative slice offset equal to zero, and the second volume has a relative slice offset (Dz) of half the slice thickness, as is shown in Figure 1 (b).

2.3 Model for fMRI data formation

Any superresolution algorithm is based on a model of the imaging process. In our case, we can easily transpose such a formalism to the MRI data formation. The physical properties of the MRI formation is well-understood [55]. Depending on the pulse sequences used for the image formation, it is a non-trivial but relatively easy task to relate the intensity measured in a voxel to the density of the proton nuclei in that voxel, weighted with their relaxation properties in the particular tissue. However, this is not very interesting for a neuroscientist. His/Her objective is to observe activated regions in the brain with functional MRI [33, 52]. Cortical brain activity which is related to a local increase in oxygenation in the activated areas, can be visualised with the "blood oxygenation level dependent contrast" technique [41] As a consequence, trying to introduce a hypothetical sophisticated model of signal formation can have the negative consequence of introducing an unexpected *bias* in the process. So it is proposed to consider a simple additive model. If $n(x)$ denotes "the activity of nuclei at position x", then the activity inside a volume v, noted $k(v)$, is given by:

$$\int_v n(x)\ dx \tag{1}$$

This model was used in many studies, and considered as a realistic assumption after comparison with experimental data [28, 43, 34].

Thus the main objective of fMRI is to acquire time series of images during different stimulation conditions and to analyse them with postprocessing software based on a general linear model described above like e.g. SPM[3] to obtain activation maps of the brain related to the tasks being performed during the experiment. It is this situation of detecting brain responses following stimulation that we will consider in this work. In particular we will show

[3]Statistical Parametric Mapping S.P.M. [16] refers to the construction and assessment of spatially extended statistical process, based on a general linear model, used to test hypotheses about neuroimaging data from SPECT/PET & fMRI. These ideas have been implemented in a software package called SPM. See also `http://www.fil.ion.ucl.ac.uk/spm/`

the interest of using superresolution techniques before performing the statistical analysis in order to improve both the spatial resolution and the statistical power of the resulting statistical parameter maps of the activated brain areas.

3 Superresolution and MRI

3.1 Notations

Let us denote by

$$l_{\mathbf{o}} = l_{(0,0,z)} \text{ with } z \in \{0 \dots Z_{\text{ratio}}\{ \tag{2}$$

the "low-resolution" data set of data-volumes where $\mathbf{o}$ denotes the low-resolution data-volume offset integer value. We will note $l_{\mathbf{o},\mathbf{i}}$, $\mathbf{i} = (u, v, w) \in \{0..X_{\text{dim}}\{\times\{0..Y_{\text{dim}}\{\times\{0..Z_{\text{dim}}\{$ the voxel index or value of the image $l_{\mathbf{o}}$.

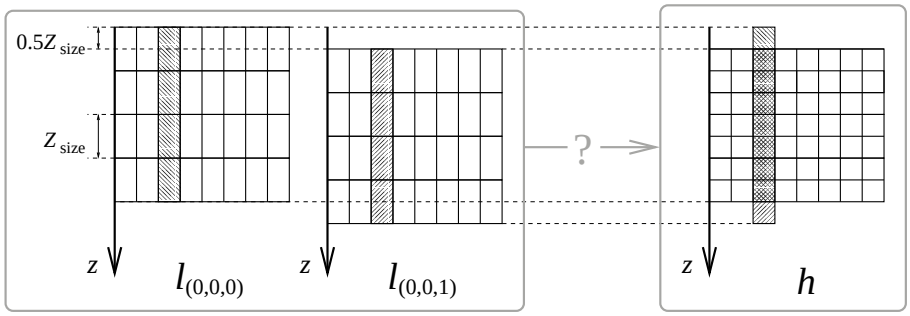

Figure 2: Example of images acquired with z offset and the expected increased resolution image. Here $Z_{\text{ratio}} = 2$.

It is supposed that these low resolution images have the following common characteristics:

- They have the same dimension $[X_{\text{dim}} \times Y_{\text{dim}} \times Z_{\text{dim}}]$ given in number of voxels.
- Voxels have the same size $[X_{\text{size}} \times Y_{\text{size}} \times Z_{\text{size}}]$ (in mm).
- Relative translations between data-volume are fixed. For a data-volume of offset $\mathbf{o}$ the relative translation is $d = (0, 0, z/Z_{\text{ratio}}\, Z_{\text{size}})$ (in mm).

From these volumes, the aim is to find a high resolution data-volume h defined as follows:

- Its dimension is $[X_{\text{dim}} \times Y_{\text{dim}} \times Z_{\text{dim}}\, Z_{\text{ratio}}]$ in number of voxels.
- Voxel size is $[X_{\text{size}} \times Y_{\text{size}} \times Z_{\text{size}}/Z_{\text{ratio}}]$ (in mm).

We will denote by h_j, where $j = (u, v, w)$, the voxel index or value. Ω will denote the spatial domain corresponding to the volumes. We also introduce two more notations:

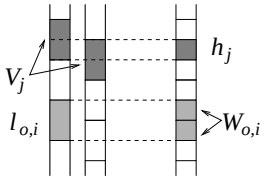

$$W_{o,i} = \{h_j / h_j \subset l_{o,i}\}$$
$$V_j = \{l_{o,i} / h_j \subset l_{o,i}\} \quad (3)$$

Now, let us consider the problem described in Figure 2 that is to compute the high resolution image from the low resolution ones.

3.2 Some simple approximations

Before setting properly the problem in terms of how low and high resolution images are linked, it may be useful to mention some easy ways to obtain increased resolution images with no efforts. This is possible in this case due to the precise sub-voxel shifts.

For instance, one may just reorganize the low resolution data as described in Figure 3.2. Note that the values of the images are not modified. The resulting image will be called in the sequel the composed image.

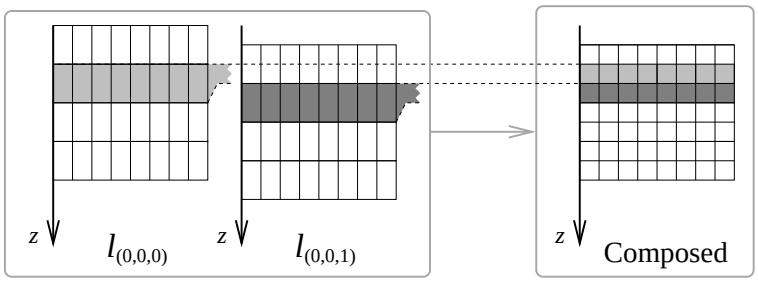

Figure 3: Composed image: this puts all the low resolution slices into the same image thus provinding a "superresolution" estimate.

Another simple way is to compute the average or mediane of every low resolution voxels containing the given high resolution voxel. For the average, this can be written by

$$h_j = \frac{1}{Z_{\text{ratio}}} \sum_{o,i \in V_j} l_{o,i}.$$

These simple ways of estimating some high resolution volume will serve as references in coming experiments (Section 4). Now, let us set properly the superresolution problem and show different ways of solving it.

3.3 Discrete least-square solution

As a consequence of (1), it is easy to establish some relations between the low and high resolution images. More precisely, we have:

$$\sum_{j \in W_{o,i}} h_j = l_{o,i} \quad \forall o, i \tag{4}$$

which is a linear system. This "conservation of intensity" is implicitly [22] or explicitly [37, 36] assumed in existing contributions. In [37] errors related to this assumption are taken into account. To solve (4), a possible solution is to consider the following optimization problem[4]:

$$\inf_h \; C(h) = \sum_{o,i} \Big(\sum_{j \subset W_{o,i}} h_j - l_{o,i} \Big)^2. \tag{5}$$

Its minimizer h will be called the least-square solution. To compute the solution one can solve the associated Euler equations:

$$\sum_{o,i \subset V_j} \Big(\sum_{j^* \subset V_{o,i}} h_{j^*} - l_{o,i} \Big) = 0 \quad \forall j. \tag{6}$$

Equation (6) can also be rewritten[5]:

$$\bar{\mu}_j(h) - \mu_j(l) = 0 \quad \text{where} \quad \left\{ \begin{array}{l} \bar{\mu}_j(h) = \sum_{o,i \subset V_j} \sum_{j^* \subset V_{o,i}} h_{j^*} \\ \mu_j(l) = \sum_{o,i \subset V_j} l_{o,i} \end{array} \right. \tag{7}$$

This is a very large sparse system of linear equations. It can be verified that it also very poorly conditioned, which means strongly noise sensitive (see [7]).

3.4 Regularizing the solution

3.4.1 General idea

To overcome the difficulty of solving (5), a common solution is to add some assumption on the regularity of the solution. This is usually done by adding some penalty term on the gradient. So it is proposed to minimize:

$$\inf_h \; E(h) = \underbrace{\sum_{o,i} \Big(\sum_{j \subset W_{o,i}} h_j - l_{o,i} \Big)^2}_{C(h)} + \underbrace{\sum_j \phi(|\delta h_j|)}_{R(h)} \tag{8}$$

where δh denotes some approximation of the gradient, the function ϕ will be determined in the sequel. To do so, we propose in the next section to review some recent work on image restoration settled in a continuous setting.

[4] This discrete formulation is very similar to the Bayesian framework where one looks for the maximum likelihood estimate (see for instance [7]).

[5] This will be used in the sequel to show the analogy with image restoration.

3.4.2 Some recalls on image restoration

Indeed, in the continuous framework, there is a very strong analogy between (8) and the variational approaches proposed in image restoration. Let us recall the problem. For a given image $h_0 : \Omega \to R$, we look for h solution of the optimization problem:

$$\inf_h \widetilde{E}(h) = \underbrace{\int_\Omega (h - h_0)^2 \, dx}_{\widetilde{C}(h)} + \underbrace{\int_\Omega \phi(|\nabla h|) \, dx}_{R(h)} \tag{9}$$

which is very similar to (8). This is a classical variational formulation which has been completely studied (see [3] for a review). Let us recall some of the main ideas:

- To determine the suitable properties for ϕ, the idea is to consider the term associated to $R(h)$ in the Euler equation:

$$(h - h_0) - \underbrace{div\left(\frac{\phi'(|\nabla h|)}{2|\nabla h|}\nabla h\right)}_{\text{diffusion operator}} = 0 \tag{10}$$

  In 3D, it can be formally shown that the diffusion operator can be rewritten as:

$$\underbrace{\phi''(|\nabla h|)}_{c_\eta} h_{\eta\eta} \; + \; \underbrace{\frac{\phi'(|\nabla h|)}{|\nabla h|}}_{c_\xi} (h_{\xi_1\xi_1} + h_{\xi_2\xi_2}) \tag{11}$$

  where $h_{\nu\nu}$ is the second directional derivative in the direction ν.[6] Thus we can impose some asymptotic conditions on the coefficients c_η and c_ξ in order to fulfill some desired behavior. For instance, in the presence of strong gradients (that is near edges) one must preserve these discontinuities. So the smoothing along η (coefficient c_η) must be suppressed (as compared to c_ξ). Notice that choosing:

$$\phi(s) = s^2 \tag{12}$$

  implies

$$c_\eta = c_\xi \equiv 1 \quad \forall h.$$

  In this case the diffusion operator is a Laplacian (an isotropic operator) and discontinuities are then lost.

  This kind of observations leads to some constraints as for the choice of ϕ and we refer to [3] for the complete study. A common suitable choice is given by:

$$\phi(s) = \sqrt{1 + s^2} \tag{13}$$

[6] The direction η is normal to the isophotes $h = cte$ and $\{\xi_i\}_{i=1,2}$ form an orthonormal basis of the tangent plane.

which is convex with linear growth at infinity. This function is like a "regularized" version of the total variation ($\phi(s) = |s|$) since it is differentiable in 0.

- The optimization problem (8) is well-posed on the space of bounded variations. Existence and uniqueness can be proven and we refer to [3] for more details.

- Using duality results is very useful to solve numerically this problem [2, 9, 4, 3]. One of the motivations is to deal with the nonlinear diffusion term (10) which comes out for suitable ϕ like (13).[7] For example, it can be shown that the problem (9) is equivalent to solve:

$$\inf_{h,b} \widetilde{E}^*(h) = \int_\Omega (h - h_0)^2 \, dx + \int_\Omega (b|\nabla h|^2 + \Psi(b)) \, dx \tag{14}$$

where Ψ is a given strictly convex function. The extra variable b is also called dual variable. The interest in the formulation (14) is twofold: this extending function is now quadratic with respect to h and the minimizer in b is in fact given explicitly. To compute the solution, an algorithm is to minimize successively with respect to each variable (see Table 1)

For (h^0, b^0) given

– $h^{n+1} = \underset{h}{argmin} \ \widetilde{E}^*(h, b^n)$. Since the problem is convex (and quadratic), this is equivalent to solving

$$\begin{cases} h - h_0 + div(b^n \nabla h) = 0 \text{ in } \Omega, \\ b^n \frac{\partial h}{\partial N} = 0 \text{ on } \partial\Omega. \end{cases} \tag{15}$$

Once discretized, the linear system can be solved with a Gauss-Seidel iterative method, for example.

– $b^{n+1} = \underset{b}{argmin} \ \widetilde{E}^*(h^{n+1}, b)$. The minimum in b is reached for

$$b^{n+1} = \frac{\phi'\left(\left|\nabla h^{n+1}\right|\right)}{2\left|\nabla h^{n+1}\right|}. \tag{16}$$

– Go back to the first step until there is convergence.

The limit (h^∞, b^∞) is the solution

Table 1: Presentation of the half-quadratic algorithm, also called ARTUR (see [8, 10]). From a numerical point of view, the only difficulty is the discretization of the term $\mathrm{div}(b\nabla u)$ in (15), where b is given and defined by (16). Several possibilities can be considered and we refer to [3] for more details.

[7] For the square function ϕ (12), the Euler equation can be easily solved since it is linear.

3.4.3 Application to our case

As noticed previously, there is a strong similarity between problems (8) and (9). Keeping the same smoothing term, the only difference comes in the equation (15) where $h - h_0$ has to be replaced by $\bar{\mu}_j(h) - \mu_j(l)$ defined in (7). A similar half-quadratic algorithm can then be used.

As far as the smoothing term is concerned, we have in fact considered two strategies:

- The first is to have a penalization on the full gradient in the three dimensions. This is exactly similar to the restoration case.
- The second is to have a penalization on the partial derivative in Z only, that is the slice direction. As the attach term only combines data along the Z direction, one may solve the problem by solving a set of 1-D independant problems with X and Y fixed and varying Z.

3.4.4 Model parameters

The numerical minimization of the energy (8) involves some parameters to be fixed by the user. They are weighting coefficients in the functional (λ and μ) placed as follows:

$$\inf_h \; E(h) = \sum_{o,i} \Big(\sum_{j \subset W_{o,i}} h_j - l_{o,i} \Big)^2 + \lambda \sum_j \phi \left(\frac{|\delta h_j|}{\mu} \right).$$

The parameter λ sets the weight of the diffusion term with respect to the attach term while the coefficient μ is a renormalization coefficient on the gradient. Such hyper-parameters can be calibrated using a reference data. Here a real high-resolution volume is considered and low-resolution synthetic data are generated from this high-resolution model using the data formation model considered in (4). Our algorithm is run and the reconstructed image is compared to the reference data. We keep the coefficients corresponding to the best reconstruction according to a given norm. Note that usually the regularization factor λ can be estimated using a technique such as L-curves [23]. (i.e. a log-log plot of the residual error for various smoothing parameter where a singularity of the curvature indicates the optimal parameter choice). Such an heuristic is not useful here since we compare our processing output with a reference data.

To summarize, we have proposed in section 3 two easy ways to have a quick estimation of a high resolution image, namely composed and average image. Next, we have properly defined the superresolution problem and introduced two different possibilities to regularize the problem (either in 3D or in the in-slice direction only, also called z-smooth). The following section will evaluate the performances of the proposed approaches with different data sets and criterions.

4 Numerical experiments

4.1 MRI of an apple

In this subsection we consider some images of an apple. The apple is frequently used as a phantom to evaluate the edge sharpness of the obtained images. High resolution datasets were acquired with a slice thickness of 1 mm and two low-resolution shifted datasets were acquired with a slice thickness of 2 mm and 3 mm respectively. The edge sharpness of the superresolution images will be compared to that of the high resolution images.

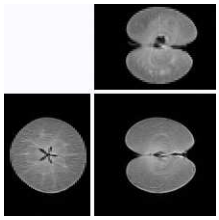

4.1.1 Materials and methods

MR images of the apple were acquired with a clinical whole-body 1.5T Siemens Sonata MR scanner. The high resolution volume and the low-resolution slice shifted volumes were acquired subsequently. The total acquisition time for the high resolution volume and for the two slice shifted volumes was set equal. The volumes were acquired with no interslice gap and all the image volumes were acquired with a standard turbo SE sequence. The machine parameters are summarize in table 2.

	High resolution	Low (2 shifts)	Low (3 shifts)
Repetition time/Echo time	3380 ms/12 ms	3380 ms/10 ms	3380 ms/9.5 ms
Turbo Factor	5	5	5
Number of Averages	32	16	12
Voxel size	$1 \times 1 \times 1$ mm	$1 \times 1 \times 2$ mm	$1 \times 1 \times 3$ mm
Acquisition matrix	128×128	128×128	128×128
Shifts	None	0 or 1 mm	0, 1 or 2 mm

Table 2: Turbo Spin Echo (TSE) imaging sequence parameters for the apple experiment

4.1.2 Results

In figures 4, 5 and 6 we qualitatively compared both the 2-shifts and the 3-shifts generated datasets with the original reference high resolution dataset and the original low resolution datasets. In Figure 4 the slices of the volume are displayed in the acquisition plane and in figures 5-6 slices are shown perpendicular to the acquisition plane.

From Figure 4 we can conclude that in the acquisition plane all the reconstructed images look quite similar with a higher SNR compared to the high resolution reference image (left top image). This is what we expected because the in-plane resolution for the original low and

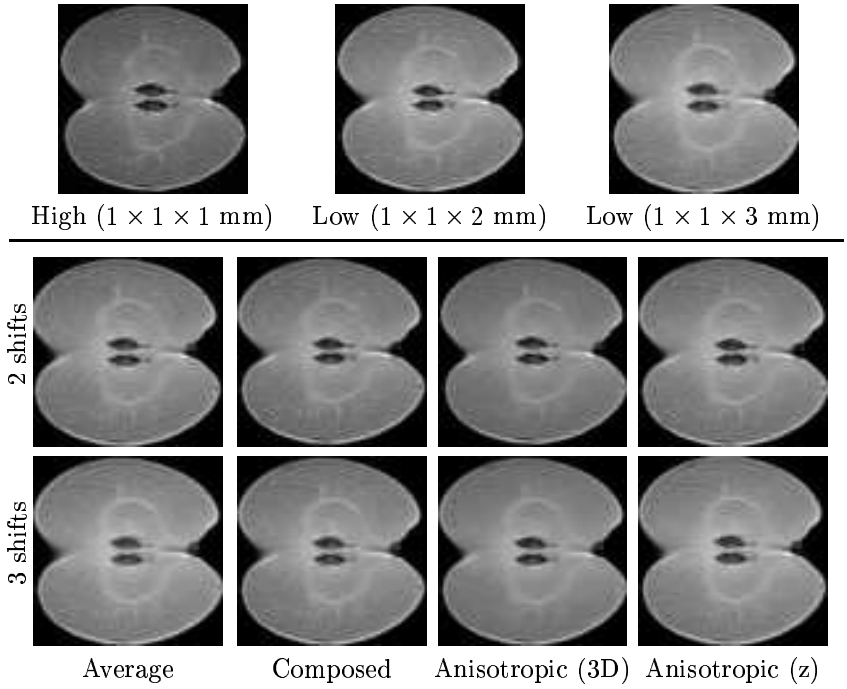

Figure 4: Transversal views of the different reconstructions. Last two rows show reconstructions obtained for 2 or 3 shifts.

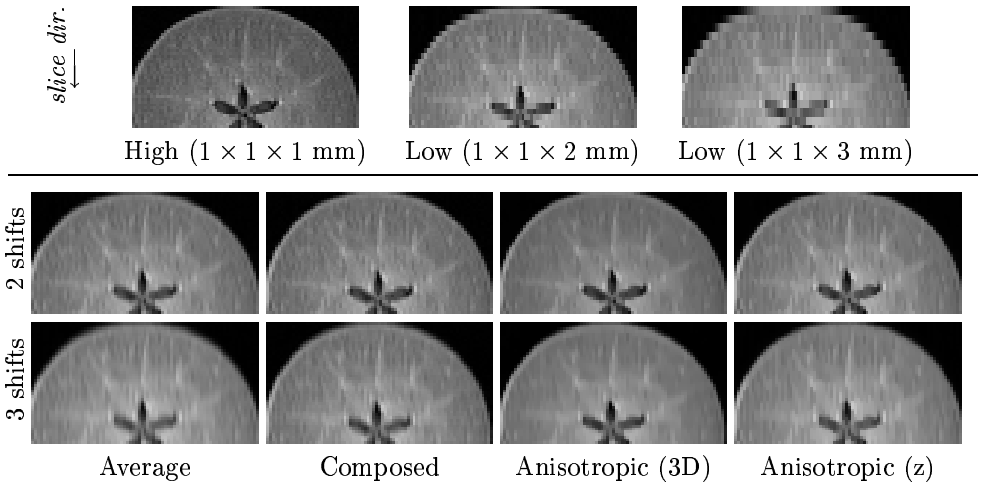

Figure 5: Coronal views of the different reconstructions. This shows the slice direction improvments. Last two rows show reconstructions obtained for 2 or 3 shifts.

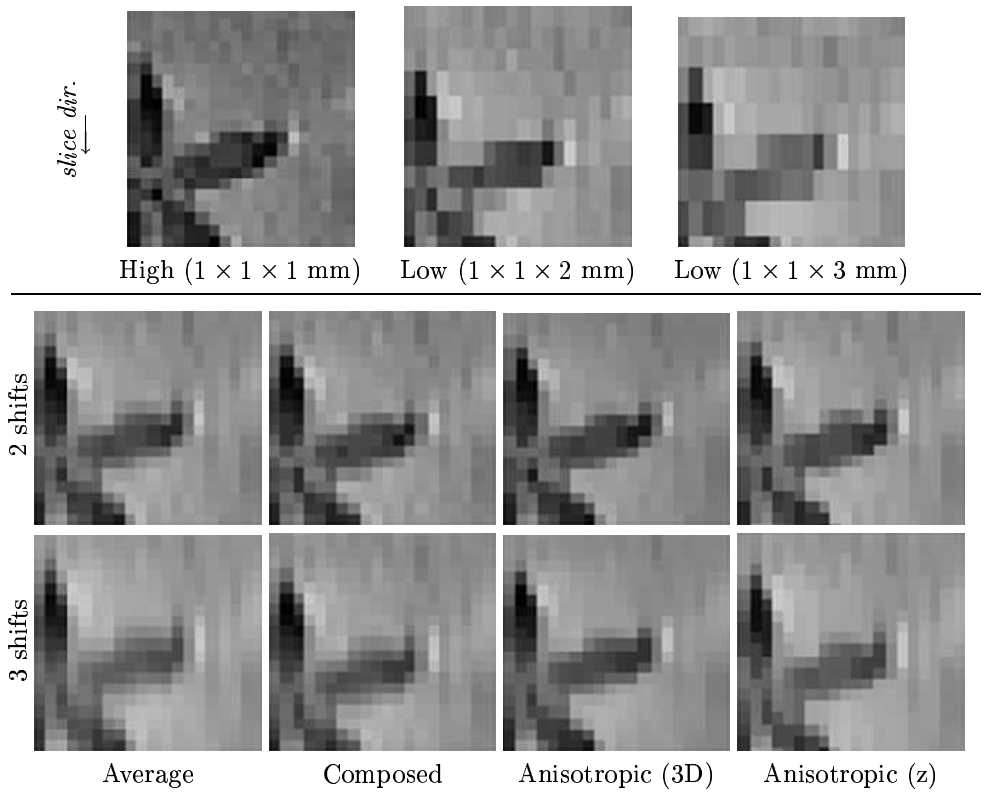

Figure 6: Close ups of coronal views of the different reconstructions. This shows the slice direction improvments.

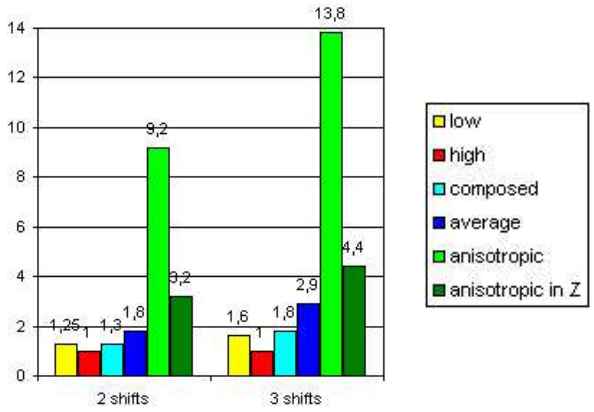

Figure 7: Relative SNR for each method and the two acquisitions.

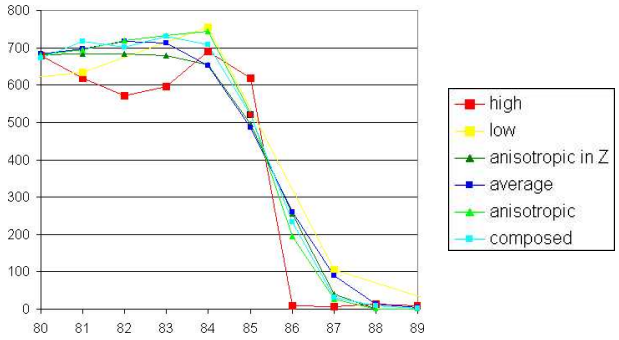

Image	Relative width [mm]
Low	9.6
High	6.45
Average	5.95
Composed	5.85
Anisotropic	5.75
Anisotropic in Z	5.73

Figure 8: Sharpness estimation based on a cut in the Z direction for the 3 shifts data sets. High resolution images are $1 \times 1 \times 1$mm. The right hand side table is a quantification of the degree of sharpness (see [21] for more details).

high resolution images were identical, thus no interpolation was performed in this direction. The anisotropic filtered image looks somewhat different displaying a much higher SNR as compared to the other images which is a result of the properties of the anisotropic diffusion filter applied in 3D.

Looking at the slices perpendicular to the acquisition plane on the other hand (figures 5-6) we observe the following differences. The original low resolution images show a clear artefact compared to the standard reference image on the left which is the result of the larger slice thickness in the low resolution images. These artefacts are clearly diminished in the interpolated images. A carefull inspection of the results shows that the diffusion filtered images (anisotropic in 3D and z-smooth) preserve best the structure of the apple, whereas the other methods show some interpolation artefacts in the slice direction. Looking at the reconstructed images, the 3 shifts datasets suffer a substantial loss of image quality and sharpness, which will make it less applicable for high resolution anatomical and fMRI studies.

Now that we have some idea of the performances of the different approaches, it would be interesting to quantify some aspects. The first would be the noise level which can be estimated through the SNR. As we do not have the ground truth in this case, the SNR is usually measured by taking the mean of high-intensity region of interest and divide it by the standard deviation of a region of noise outside the image of the object [22]. The results are shown in Figure 7. The histograms essentially show a much higher SNR improvement for the anisotropic cases as compared to the other interpolation techniques and the original high resolution images[8] Measured relative SNR values for the slice shifted datasets are compared with the high resolution standard dataset in Figure 7. The results show a SNR rise ranging from a factor of 1.34 to 9.19 for the 2-shifts dataset and 1.84 to 13.83 for the 3-shifts dataset. This graphs clearly demonstrate that the methods using diffusion (anisotropic in 3D and

[8]The high resolution images are taken with 2 to 3 times the amount of averages compared to the 2 resp. 3 shifts datasets. The reason was to keep the same total acquisition time for each volume.

z-smooth) show the largest, most spectacular increase in measured SNR which is a result of the inherent filter characteristics of these methods.

Finally, it is interesting to estimate edge sharpness which is a quality criterion. This can be done by comparing cuts of the different reconstructions in a neighborhood of a sharp intensity variation in the slice direction. Results are shown in figure 8. To better quantify these results, we used a mathematical formula to estimate the edge width (see [21] for more details). It appears that anisotropic smoothing techniques allow sharper edges reconstructions.

4.2 Anatomical MRI of a human brain

In this subsection we consider different "anatomical" MRI datasets of a human brain acquired with several different imaging sequences and parameters. High-quality "anatomical" datasets were acquired with a TSE sequence to evaluate the anatomical sharpness and quality of the interpolated data generated by the superresolution algorithms. Other datasets were acquired with the EPI sequence also used in the fMRI protocol in order to calibrate the superresolution algorithm for the generation of the best possible new interpolated fMRI datasets.

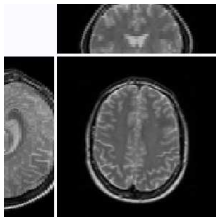

4.2.1 Materials and methods

Various MR image volumes of the brain of a normal human volunteer were acquired with a clinical whole-body 1.5T Philips Intera scanner. For all sequences and parameter settings, the high resolution and slice-shifted volumes were taken from the same head volume. The total acquisition time for the high resolution set and for the slice shifted sets was equal. All acquisitions were performed with no interslice gap. We used Standard TSE for the acquisition of the high resolution and slice-shifted MRI volumes. The parameters settings are given in table 3.

	High resolution	Low resolution
Repetition time/Echo time	2500 ms/26.7 ms	2500 ms/26.7 ms
Turbo Factor	5	5
Number of Averages	2	1
Voxel size	$(1.72)^3$ mm	$1.72 \times 1.72 \times 3.44$ mm
Acquisition matrix	128×128	128×128
Number of slices	40	24
Shifts	None	0 or 1.72 mm

Table 3: Turbo Spin Echo (TSE) imaging sequence parameters for the apple experiment

4.2.2 Results

From the human anatomical data (see figures 9–11) the same conclusion can be drawn as from the apple data. The anisotropic images and the z-smooth images both show the best results in maintaining the anatomical properties of the data in the in-plane direction and perpendicular to the slice direction. The other techniques show on the sagittal and coronal images perpendicular to the slice direction small interpolation artefacts (some zebra pattern can be observed a some scale) as is also observed in the apple data. The SNR of the images behaves in a similar manner as those of the apple data, showing the largest gain in SNR in the images generated by the diffusion algorithms.

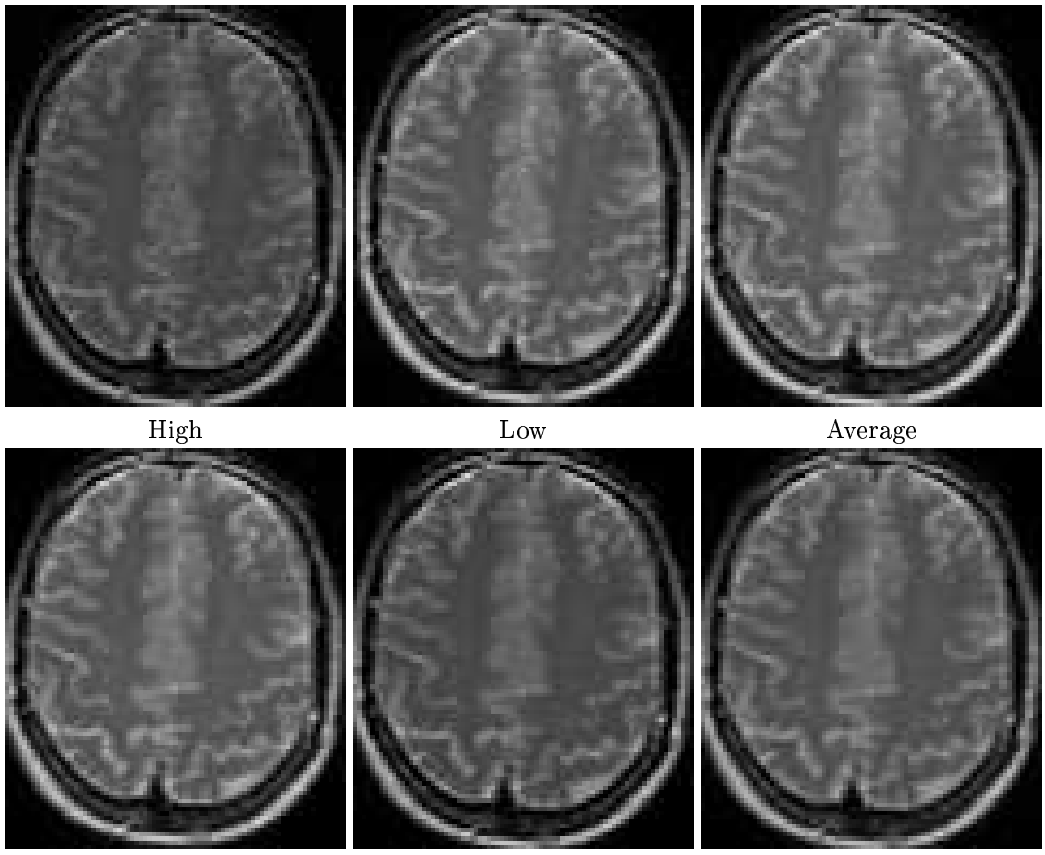

Figure 9: Transversal views of the different reconstructions.

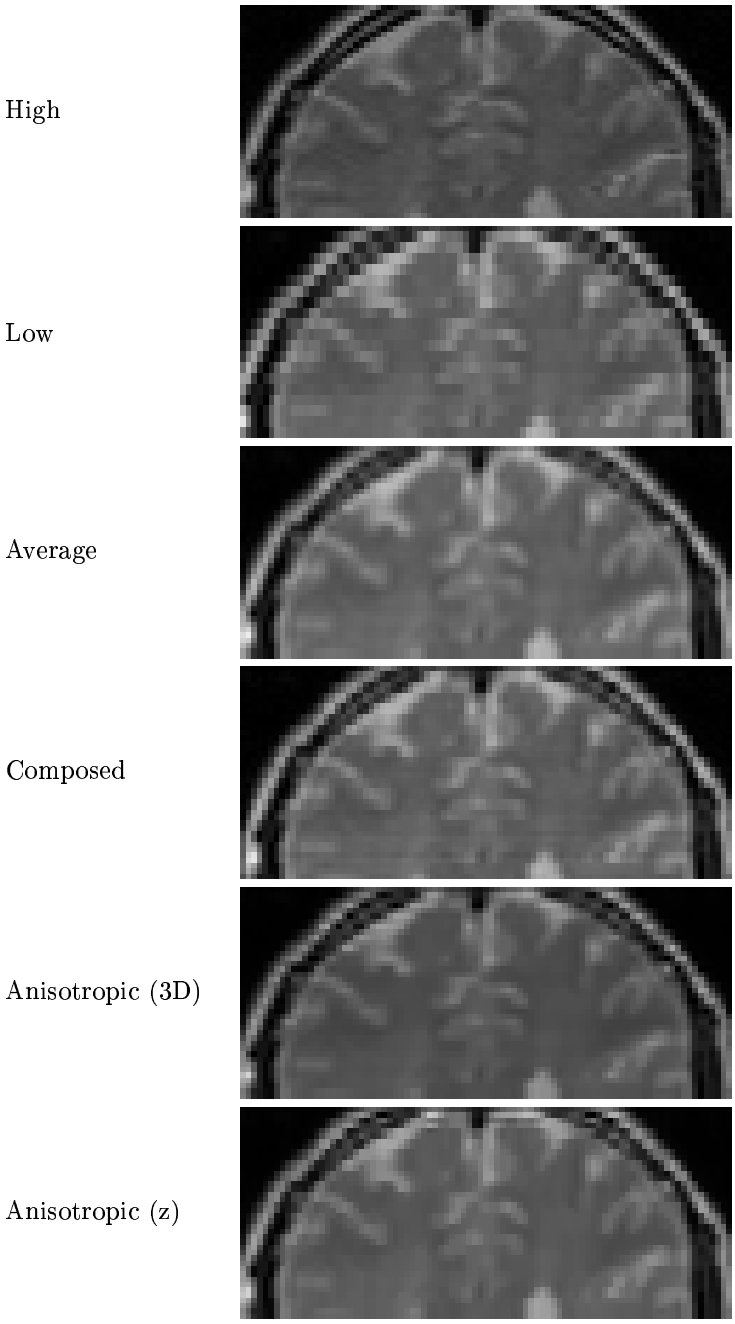

Figure 10: Coronal views of the different reconstructions. It shows cuts in the in-slice direction to estimate the increase of resolution.

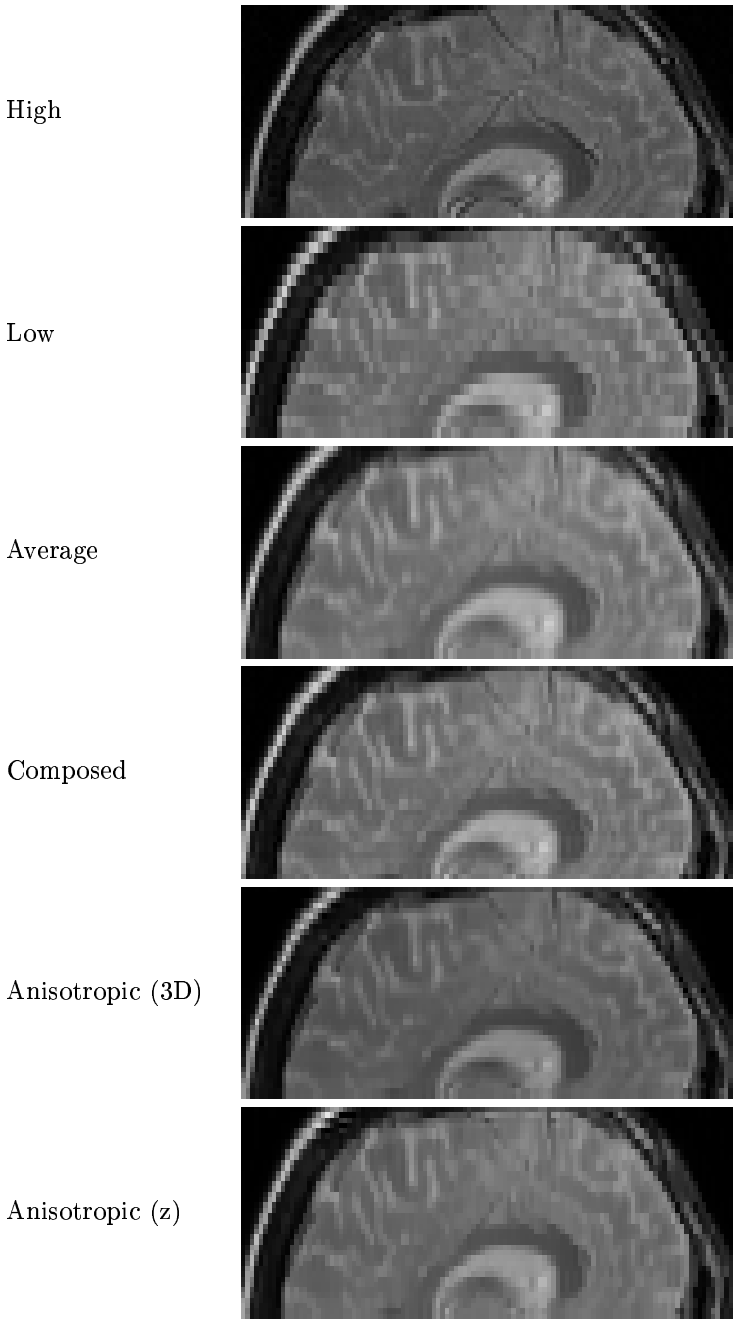

Figure 11: Sagittal views of the different reconstructions. It shows cuts in the in-slice direction to estimate the increase of resolution.

4.3 fMRI time series on human volunteers

In this subsection the superresolution algorithms were tested on real fMRI datasets, after optimisation on the human anatomical data of the previous section. Different datasets were acquired:

- High resolution volumes as the ground truth for comparison of the activated areas with those of the superresolution datasets.
- Slice-shifted volumes with the double slice thickness to create the superresolution datasets.

4.3.1 Materials and methods

Two neurophysiological stimulation paradigms were used in the experiments:

- Motor paradigm. In this experiment a simple motor paradigm designed to activate the motor cortex was used, consisting of 3 conditions implemented in four alternating MRI acquisition "blocks" consisting of rest, finger tapping, rest and toe movement. Every block lasted for 10 brain volume scans. One session consisted of 8 blocks, i.e., 80 scans, thus in one session every condition was repeated twice, this paradigm is shown in figure 12 (a). During the experiment a total of ten scanning sessions were performed on the same subject, 5 sessions for acquiring the high resolution volumes and 5 sessions for the acquisition of the slice-shifted low resolution volumes. The images were collected on a Philips Intera 1.5T system.
- Visual paradigm. The stimuli used in the visual retinotopic mapping experiment were designed to stimulate the horizontal and vertical visual field meridian. The horizontal (HM) and vertical (VM) meridian stimuli were horizontally and vertically oriented wedge-shaped checkerboards. The width of the wedges was 15° within each hemisphere, resulting in a width of 30° for the vertical meridian stimulus. All retinotopic stimuli were checkerboards that consisted of black and colored checks, which alternated at 4 Hz. The HM and VM were alternated in blocks, every block consisted of 10 brain volume scans. The paradigm is shown in figure 12 (b). In this experiment a total of 10 sessions of 12 blocks each, i.e., 120 scans per session were performed on the same subject, yielding 5 high resolution and 5 slice-shifted low resolution volume datasets. The images were collected on a Siemens Sonata 1.5T system.

4.3.2 Postprocessing of the acquired dataset

The processing of the functional MR images is performed with the aid of a number of procedures which are all implemented in the SPM99 package. This postprocessing can be divided into two major parts. The first deals with the spatial preprocessing of the images and the second part is the actual statistical analysis of the data. The spatial preprocessing of the dataset consists of the following steps:

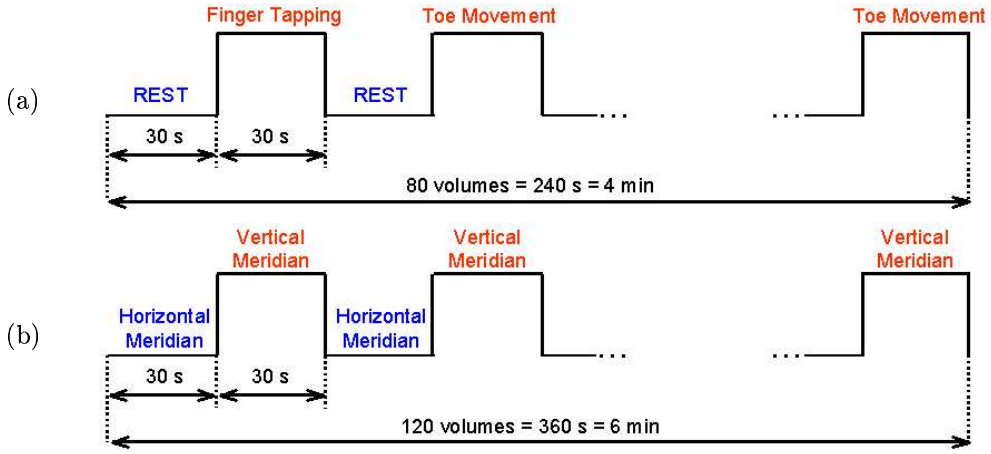

Figure 12: The two different stimulation paradigms: (a) the motor paradigm and (b) the visual paradigm

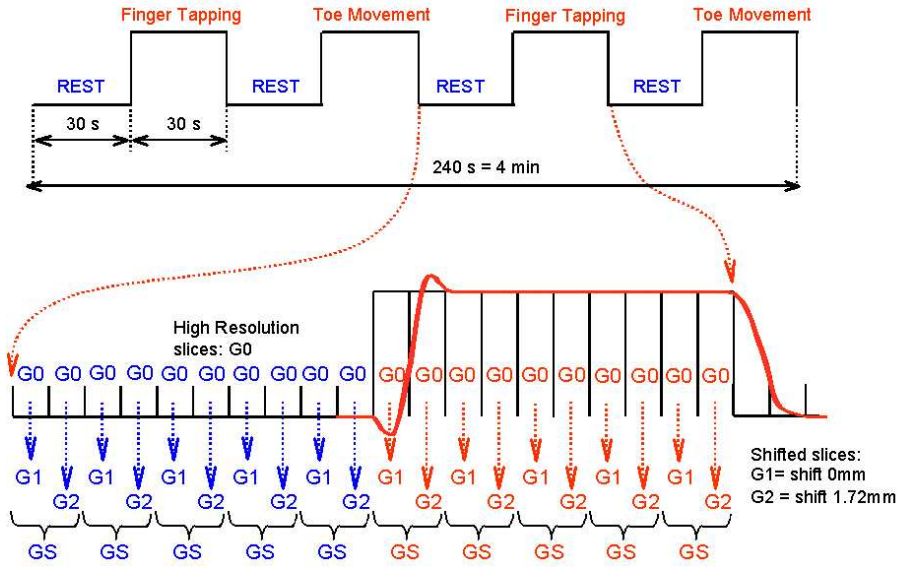

Figure 13: The two different acquisition protocols, high resolution (G0) and slice shifted (G1 and G2 for the non-shifted and the shifted slices, which are interpolated to a new superresolution dataset GS) in the motor fmri protocol are displayed. In the upper part the entire stimulation paradigm is shown and in the lower part two consecutive blocks are shown in detail. The expected hrf function in the activated voxels is drawn on top of these blocks. Notice the loss of temporal information in the superresolution dataset. G0,G1,G2 as defined in figure 1

	Motor paradigm		Visual paradigm	
	High	Low	High	Low
Repetition time/Echo time	5180 ms/48 ms	5180 ms/48 ms	3328 ms/54 ms	3328 ms/54 ms
Number of Averages	1	1	1	1
Number of scans	80	80	120	120
Voxel size	$(1.72)^3$ mm	$1.72 \times 1.72 \times 3.44$ mm	2^3 mm	$2 \times 2 \times 4$ mm
Acquisition matrix	128×128	128×128	128×128	128×128
Shifts	None	0 or 1.72 mm	None	0 or 2 mm
Number of slices	22	11	32	16

Table 4: Imaging sequence parameters for the FEEPI sequence used in the fMRI time series experiments.

- Motion correction. Human fmri data is always corrupted with bulk head motion. An fmri experiment typically lasts for about 6 minutes, during this time it will be very difficult to constrict the head motion to less than 1 mm. The motion manifests itself as a slow drift of the brain in different translation and rotation directions during one session and a possible translation and rotation offset between sessions. If the datasets are not corrected for this head motion the final results obtained after the statistical analysis will be largely contaminated with false positives and negatives. The correction of this head motion is achieved by a rigid realignment of the consecutively acquired volumes in the data series to the first image [18].

- Spatial smoothing. The image volumes are spatially smoothed by convolving the datasets with an isotropic Gaussian kernel. This smoothing leads to an increased spatial SNR of the datasets. To obtain the best results, the width of the Gaussian kernel has to be matched to the spatial extent of the expected activated areas. In the present experiments we used a Gaussian kernel of $(3 \text{ mm})^3$. These preprocessing steps were identical for both the high resolution reference and the interpolated superresolution datasets.

After these preprocessing steps the actual statistical analysis can be performed on the different datasets. The standard statistical analysis uses the General Linear Model (GLM) which decomposes the measured signal intensity of each voxel into different components, such as the stimulus driving function, and the slow drift resulting from small global physiological changes. This resulting model is further convolved with the haemodynamic response function (hrf), which describes the temporal characteristics of the haemodynamic response in the brain following neural activation. Thus in the standard fMRI data analysis with SPM, the temporal characteristics of the measured and the expected signal changes are both taken into account [17].

As a result of the loss of the temporal information in the slice-shifted acquisition mode of the data (figure 13), it is not possible to use the standard SPM statistical analysis protocols. Figure 13 displays the hrf and the acquisition protocol for the motor paradigm and shows that the image data acquired during the initial and final portion of the hrf are not in the stationary

state (plateau) of the hrf and cannot be used for the post-hoc superresolution algorithm which combines sets of shifted and non-shifted volumes acquired in identical stimulated conditions. the standard statistical analysis techniques used for fmri data thus cannot be applied on the interpolated superresolution datasets. Instead we generated the fMRI design matrix by using the box car function only, without convolving it with the haemodynamic response function. In the analysis we discarded the first image volumes (G0 for the high resolution, and G1 and G2, for the low resolution) of every condition. As a result this analysis technique, which assumes a block model, is not as powerful as the standard fmri analysis model used in SPM, and will lead to suboptimal results. In order to compare the different acquisition protocols, the high resolution reference datasets are analysed both with the standard fMRI statistics and the adapted simplified statistics toolboxes, using SPM, and the superresolution datasets are analysed only with the simplified design matrix in SPM. Note: The data of the simplified statistics for the high resolution datasets are not shown in the activation maps, but their quantitative measurements are shown in the graphs.

4.3.3 Results

In this section we describe the results obtained with the SPM data analysis of the different interpolated and original datasets. In order to rank the different superresolution techniques by power and correctness, we performed both a qualitative as well as a quantitative comparison between the different resulting activation maps.

Qualitative analysis

In order to analyse the data qualitatively we generated different SPM activation maps, displaying the activated areas which are above the statistical threshold (p_{corr} <0.05) overlaid on the mean EPI slices of the interpolated datasets. Figures 14 and 15 show several slices of the different datasets both for the motor task (figure 14: Activated areas resulting from the fingertapping as compared to rest) as for the visual retinotopic mapping paradigm (figure 15: Areas responding to vertical meridian stimuli and responding to horizontal meridian stimuli). Figures 14A and 15A display slices in the acquisition direction with the corresponding activation overlaid and figures 14B and 15B display them perpendicular to the slice direction. Globally all the activation maps of the interpolated datasets have a largely similar look as compared to each other and to the high resolution reference dataset both for the motor and the visual tasks. But when looking at the data in more detail we observe that the interpolated datasets show a higher t-value at the foci of the different activated areas as compared to the reference and the low resolution dataset. As a result of this also larger activated areas showing a t-value above threshold are observed in the interpolated datasets compared to the original data. When comparing the different interpolated datasets in both studies we observe the following differences. In both studies the 3D anisotropic images display more intense but also less sharp activation patches as compared to the other interpolated datasets. This is probably the result of the filtering inherent to the 3D anisotropic interpolation algorithm. The results obtained with the other 3 interpolation algorithms are all very

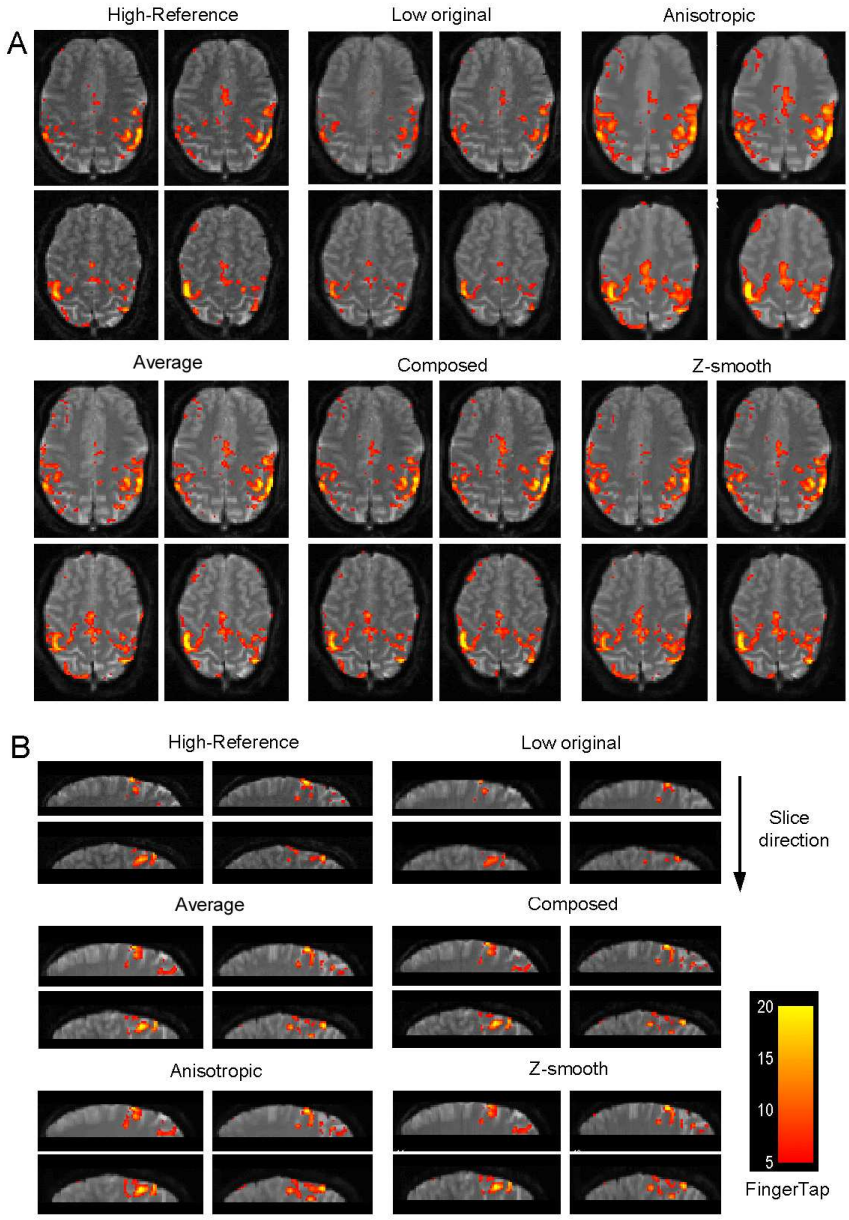

Figure 14: Slices of activated areas resulting from bimanual finger tapping overlaid on the mean EPI images for the different interpolated datasets. In A slices are displayed in the transversal plane and in B sagittal slices are shown. The t-value threshold ranges between 5 (red) and 20 (yellow) as is shown in the accompanying the colour bar.

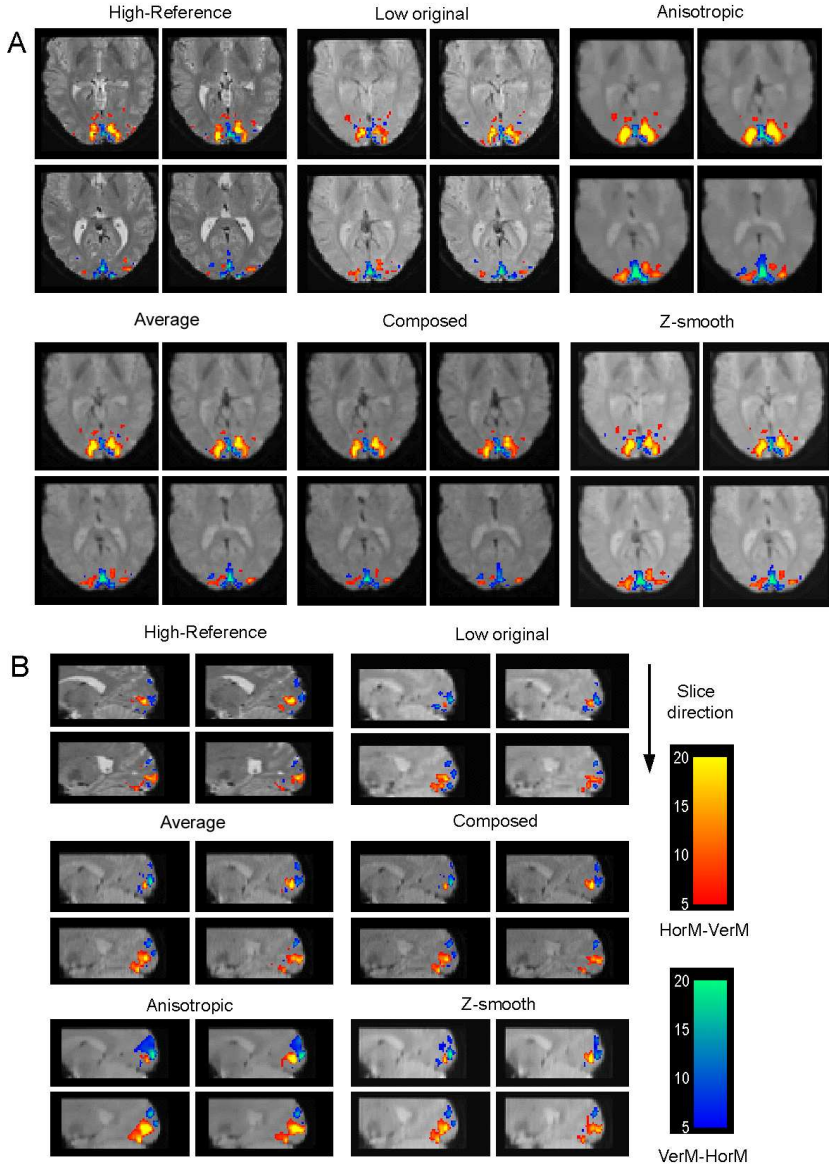

Figure 15: Slices of activated areas resulting from the visual stimulation paradigm overlaid on the mean EPI images for the different datasets. In A slices are displayed in the transversal acquisition plane and in B sagittal slices are shown. Two different colour bars are used, in both colour bars the t-value threshold ranges between 5 and 20. In the red to yellow colour the horizontal meridian stimulation against the vertical meridian stimulation is shown and in the blue to green colour the opposite effect is shown (vertical meridian against horizontal meridian).

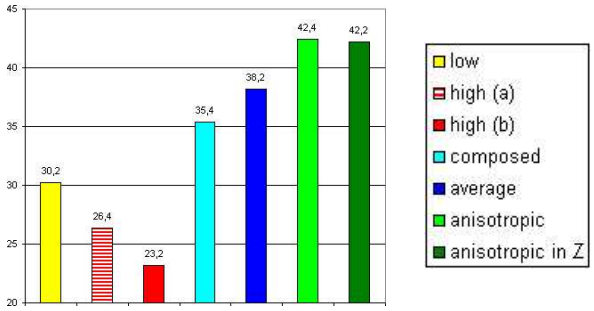

Figure 16: Bar graph of the maximal t-value in the activated areas for the low resolution, the high resolution analysed with the standard model (b) and analysed with the adapted model (a) and the 4 interpolated datasets.

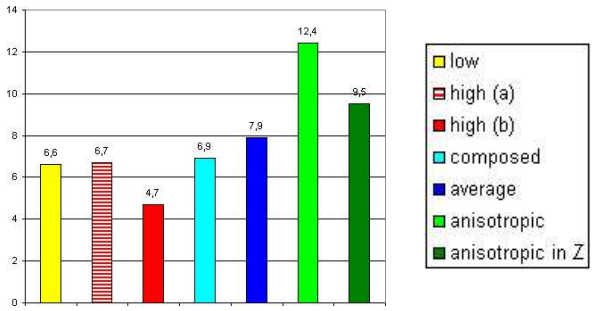

Figure 17: Bar graph of the total activated volume above the p_{corr} threshold of 0.05 for the low resolution, the high resolution analysed with the standard model (b) and with the adapted model (a) and the 4 interpolated datasets.

similar with a slightly higher intensity of the activated patches in the z-smoothed dataset. But it is very difficult to mark the best interpolation technique in the qualitative analysis, therefore we performed some quantitative analysis to obtain an objective measurement of which superresolution algorithm returns the best results in the activation maps.

Quantitative analysis

In order to have a more objective comparison between the different techniques we performed different quantitative measurements on the resulting SPMs. The following quantitative measurements were performed: The measurement of the highest global t-score value observed in the activated areas of the entire dataset and the calculation of the total number of activated voxels above the p_{corr} value of 0.05 across all remaining clusters larger than 20 voxels in the motor paradigm and 10 voxels in the visual paradigm. The results of these measurements are displayed in figures 13 and 14 for the visual retinotopic mapping paradigm.

The measurements in the motor task datasets generated very similar graphs as for the visual task both for the maximal t-value observed as for the number of activated voxels. In figure 13 the maximal measured t-value in the activated areas is shown for the horizontal meridian stimuli minus the vertical meridian stimuli. All four the superresolution datasets generated higher maximal t-values as compared to the high resolution reference data set analysed with the 2 different statistical models and the original low resolution datasets. We also observed that the anisotropic dataset generated the highest t-score followed by the z-smooth, average and composed datasets respectively. In figure 14 the activated volume above threshold is plotted for all datasets. Again we observe that the interpolated datasets generated a much larger total volume of activation above threshold and also that the anisotropic dataset has the largest volume of activation. These quantitative measurements suggest that the anisotropic dataset is the one displaying both the largest significance and the largest detectability of the activated areas, followed by the z-smooth, average and composed datasets respectively.

Taking into account both the results of the qualitative and the quantitative analysis we can conclude that although the anisotropic superresolution dataset displays the best quantitative results it is much more smoothed as compared to the others. Therefore the z-smooth dataset looks like a good compromise if one wants to detect small activated areas with a high resolution. But if one wants to increase detectability of large activated areas the anisotropic dataset appears to be the best solution.

Finally, we may also notice that the anisotropic smoothing in 3D introduces (by definition) a spatially non-uniform noise smoothing. Figure 18(a) shows such a noise image of the anisotropic superresolution dataset. The non-uniform smoothing effects are easily observed in the white matter of the brain, which is strongly and uniformly smoothed, while in the grey matter the smoothing is much less due to the presence of the image intensity variations from the sulci and gyri structures. This non uniform spatial smoothing imposes a spatial variation of the t-values of the observed activated regions calculated by SPM and thus could alter the SPM values map, which won't be acceptable. But if we stick only to the grey matter, the differences in smoothness for the different parts of the gray matter are only small which will then result in a more uniform spatial smoothing making it perhaps acceptable for the SPM statistics. Since the slice-shifted acquisition subsamples the image space only in the slice direction and the corresponding spatial interpolation should only take place in that slice direction. It won't be necessary to use the anisotropic smoothing in 3D, which could introduce different artifacts in the corresponding calculated SPM maps as a result of the nonisotropic smoothing effects. Therefore we prefer to only apply this technique in the slice direction and to apply the commonly used local Gaussian smoothing in 3D of the datasets before the SPM calculation, which will lead to an isotropic distribution of the noise in the images. Figure 18(b) shows the noise image of the z-smoothed dataset, demonstrating a much more homogeneous noise distribution for the entire brain, making the results of this technique more suitable to calculate the SPM statistics.

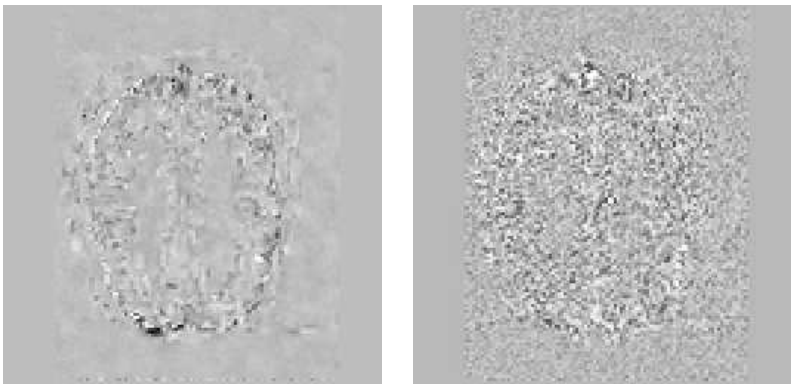

(a) (b)

Figure 18: Comparison of residual noise on interpolated data sets with (a) anisotropic diffusion in 3D and (b) diffusion only in the in-slice direction.

5 Conclusion

This work investigated the possibility to use superresolution techniques in fMRI studies. We wanted to define a protocol capable of enhancing the resolution to be able detect very small activated areas. In order to solve this problem a regularization method had to be constructed which allows to smooth the reconstructed image while keeping its main discontinuities. It is proposed to penalize either the full gradient in 3 dimensions or the gradient along the slice direction only, which allows a very efficient implementation. These techniques have been compared to other straightforward data interpolation techniques. In order to compare these techniques it is very important to perform a real life comparison between the different results in anatomical images and in different actual fMRI experiments.

In the first step we started with an estimation of the correctness of the different approaches applied to single sets of different slice shifted images by comparing the results with the real high resolution data. In a second step the different superresolution techniques were evaluated in some real fMRI experiments in connection with the detection of activated areas in the brain of human subjects performing several different tasks.

From the visual and quantitative analysis of the apple and anatomical data we can draw the following conclusions. The use of the superresolution technique on the MR images greatly improves the signal to moise ratio (SNR) of the interpolated images as compared to both the standard reference images and also to the original shifted low resolution images. This improvement in SNR for all the superresolution images as compared to the reference image is partly the result of the larger voxel size of the acquired images. The SNR enhancement in the mean interpolated images as compared to the low resolution and the composed superresolution images is the result of the averaging performed in this technique. Both the anisotropic superresolution imagesets (3D and slice direction only) display an even larger

SNR improvement. This improvement was expected because it is inherent to the algorithm used for the generation of these superresolution images. One can also clearly observe that when performing this interpolation in the 3 directions the gain in SNR is approximately 3 times higher as compared to the application of the same technique in the slice direction only.

When estimating the sharpness of the apple images in the slice direction we found that the interpolated images have a better edge sharpness as compared to the low resolution images as expected but that they even display unexpected sharper edges than the reference high resolution images. This amelioration is probably the result of the gain in SNR in the interpolated images as compared to the standard high resolution dataset. Comparing the different superresolution images we observe the sharpest edges in both the anisotropic volumes. When performing a visual analysis of the data, the different interpolated datasets show a similar quality. There are some interpolation artifacts visible in the slice direction, these artifacts are the largest in the composed datasets and in the anisotropic superresolution volumes these artifacts are much smaller. Thus both from the apple and anatomical data we can conclude that from the different interpolation techniques, the anisotropic technique in 3D generate the best quality datasets in terms of slice interpolation artifacts, SNR and edge sharpness.

After these tests on the anatomical and apple data we also performed some real fMRI experiments on human volunteers in order to compare the activation maps generated from the interpolated datasets with each other and with a reference high resolution dataset. In order to compare the different methods we performed a visual qualitative analysis as well as a quantitative analysis of the obtained activation maps. In the qualitative analysis we observed a gross resemblance between the observed activated areas of the reference dataset and the interpolated datasets, where the superresolution datasets show larger areas above statistical significance threshold. This is the result of the higher SNR observed in the superresolution images. When comparing the activation maps of the different superresolution datasets we found that the 3D anisotropic case shows a more smoothed pattern of activation resulting in a loss of sharpness in the different activated patches as compared to the other interpolation techniques. This smoothing is again the result of the properties of the anisotropic diffusion filter. The quantitative analysis on the other hand demonstrated that the 3D anisotropic dataset generated the highest t-values for the activated areas and the largest areas above activation threshold. This result was expected as these images have the largest SNR value which results in a larger statistical significance for the activated areas.

Taking together both the results of the qualitative and the quantitative analysis of the activation maps we could come to the following general conclusions. The 3D anisotropic dataset shows the highest level of activation but loses some resolution and sharpness in the activated areas. This technique will be very suitable if one wants to observe large activated areas and there is no need for a sharp delineation of the boundaries of the activated regions or if one performs a group analysis pooling several different subjects together. Because in this case one always needs to smooth the datasets in order to eliminate the individual differences between the subjects. In both these cases the spatial resolution of the 3D anisotropic interpolation technique would be optimal. If one wants to observe small activated regions

with a very high resolution the 3D anisotropic technique will be suboptimal, therefore the anisotropic interpolation technique in the slice direction only would be the best alternative. With this technique the gain in SNR won't be as large as in the full anisotropic dataset but it is still much larger as compared to the other interpolation techniques. In the datasets generated with this technique the sharpness of the activated areas is similar as in the other techniques, but the statistical significance of the activated pixels is higher, which makes this technique as a good candidate to find the activated areas with a high spatial resolution.

Acknowledgments. This work was partially funded by European project MAPAWAMO (ref. QLG3-CT-2000-30161; coordinator: Pr. Guy Orban, Lab. of Neuro- and Psychophysiology, Dept. of Neurosciences and Psychiatry, K.U. Leuven, Belgium). We would like also to thank Rachid Deriche and Mila Nikolova for their useful comments and suggestions.

References

[1] K. Aizawa, T. Komatsu, and T. Saito. Acquisition of very high resolution images using stereo cameras. In *SPIE Visual Communications and Image Processing*, volume 1605, pages 318–328, Boston, MA, 1991.

[2] G. Aubert, L. Blanc-Féraud, M. Barlaud, and P. Charbonnier. A deterministic algorithm for edge-preserving computed imaging using Legendre transform. In *Proceedings of the International Conference on Pattern Recognition*, volume III, pages 188–191, Jerusalem, Israel, October 1994. Computer Society Press.

[3] G. Aubert and P. Kornprobst. *Mathematical Problems in Image Processing: Partial Differential Equations and the Calculus of Variations*, volume 147 of *Applied Mathematical Sciences*. Springer-Verlag, December 2001. Utiliser aubert-kornprobst:02.

[4] G. Aubert and L. Vese. A variational method in image recovery. *SIAM Journal of Numerical Analysis*, 34(5):1948–1979, 1997.

[5] S. Baker and T. Kanade. Limits on super-resolution and how to break them. In *Proceedings of the International Conference on Computer Vision and Pattern Recognition*, Hilton Head Island, South Carolina, June 2000. IEEE Computer Society.

[6] B. Bascle, A. Blake, and A. Zisserman. Motion deblurring and super-resolution from an image sequence. In Bernard Buxton, editor, *Proceedings of the 4th European Conference on Computer Vision*, pages 312–320, Cambridge, UK, April 1996.

[7] D. Capel and A. Zisserman. Super-resolution enhancement of text image sequences. In *Proceedings of the International Conference on Computer Vision and Pattern Recognition*, Hilton Head Island, South Carolina, June 2000. IEEE Computer Society.

[8] P. Charbonnier. *Reconstruction d'image: régularisation avec prise en compte des discontinuités*. PhD thesis, Université de Nice-Sophia Antipolis, 1994.

[9] P. Charbonnier, G. Aubert, M. Blanc-Féraud, and M. Barlaud. Two deterministic half-quadratic regularization algorithms for computed imaging. In *Proceedings of the International Conference on Image Processing*, volume II, pages 168–172, 1994.

[10] P. Charbonnier, L. Blanc-Féraud, G. Aubert, and M. Barlaud. Deterministic edge-preserving regularization in computed imaging. *IEEE Transactions on Image Processing*, 6(2):298–311, 1997.

[11] W.A. Edelstein, J.M. Hutchinson, G. Johnson, and T. Redpath. Spin warp nmr imaging and applications to human whole body imaging. *Phys Med Biol*, 25(4):751–756, 1980.

[12] M. Elad and A. Feuer. Super-resolution reconstruction of continuous image sequence. *IEEE Transactions on Pattern Analysis and Machine Intelligence*, 21(9):817–834, 1999.

[13] J.M. Ellermann, D. Flament, S.G. Kim, Q.G. Fu, H. Merkle, T.J. Ebner, and K. Ugurbil. Spatial patterns of functional activation of the cerebellum investigated using high field (4T) MRI. *NMR Biomed*, 7:63–68, 1994.

[14] H. Fischer and R. Ladebeck. Echo-planar imaging image artifacts. In et al. F. Schmitt, editor, *Echo-Planar Imaging, Theory, Technique and application.*, pages 191–200. Springer, Heidelberg, 1998.

[15] B. Frieden and H. Aumann. Image reconstruction from multiple 1-d scans using filtered localized projection. *Applied Optics*, 26:3615–3621, 1987.

[16] K.J. Friston, J. Ashburner, et al. *spm 97 course notes*. Wellcome Department of Cognitive Neurology, University College london, 1997.

[17] K.J. Friston, A.P. Holmes, J.B. Poline, P.J. Grasby, S.C. Williams, R.S. Frackowiak, and R. Turner. Analysis of fMRI time series revisited. *Neuroimage*, 2:45–53, 1995.

[18] K.J. Friston, S. Williams, R. Howard, R.S. Frackowiak, and R. Turner. Movement related effects in fMRI time-series. *Magn Res Med*, 35:346–355, 1996.

[19] S. Gold, R. Christian, S. Arndt, G. Zeien, T. Cizadlo, D.L. Johnson, M. Flaum, and N.C. Andreasen. Functional mri statistical software packages: a comparative analysis. In *Human Brain Mapping*, volume 6, pages 73–84, 1998.

[20] G.H. Golub. Some modified matrix eigenvalue problems. *SIAM Review*, 15:318–334, 1973.

[21] H. Greenspan, G. Oz, N. Kiryati, and S. Peled. Super-resolution in MRI. *IEEE Trans. on Medical Imaging*, 2001. Submitted.
`http://www.eng.tau.ac.il/ñayit/publications/MRI_paper_submit.ps.gz`,

[22] H. Greenspan, S. Peled, G. Oz, and N. Kiryati. MRI inter-slice reconstruction using super-resolution. In *Medical Image Computing and Computer-Assisted Intervention-MICCAI 2001*, volume 2208 of *Lecture Notes in Computer Science*, pages 1204–1206. Springer, 2001.

[23] P.C. Hansen. The l-curve and its use in the numerical treatment of inverse problems. In P. Johnston, editor, *Computational Inverse Problems in Electrocardiology,*, pages 119–142, 2001.

[24] F.G. Hoogenraad, M.B. Hofman, P.J. Pouwels, J.R. Reichenbach, S.A. Rombouts, and E.M. Haacke. Sub-millimeter fMRI at 1.5 Tesla: correlation of high resolution with low resolution measurements. *J Magn Reson Imaging*, 9(3):475–482, March 1999.

[25] M. Irani and S. Peleg. Improving resolution by image registration. *CVGIP: Graphics Models and Image Processing*, 53:324–335, 1993.

[26] M. Irani and S. Peleg. Motion analysis for image enhancement: resolution, occlusion, and transparency. *Journal on Visual Communications and Image Representation*, 4(4):324–335, 1993.

[27] Anil K. Jain. *Fundamentals of Digital Image Processing.* Prentice-Hall International Editions, 1989.

[28] C. Janz, S.P. Heinrich, J. Kornmayer, M. Bachand, and J. Hennig. Coupling of neural activity and BOLD fMRI response: new insights by combination of fMRI and VEP experiments in transition from single events to continuous stimulation. *Magn Reson Med*, 46(3):482–486, September 2001.

[29] D.A. Kelley and J.F. Schenck. Very-high-field magnetic resonance imaging: instrumentation and safety issues. *Top Magn Reson Imaging*, 10(1):79–89, February 1999.

[30] S.P. Kim, N.K. Bose, and H.M. Valenzuela. Recursive reconstruction of high resolution image from noisy undersampled multiframes. *IEEE Transactions on Acoustics, Speech, Signal Processing*, 38(6):1013–1027, 1990.

[31] A. Kumar, D. Welti, and R.R. Ernst. NMR Fourier zeugmatography. *J Magn Reson*, 18(1):69–83, 1975.

[32] P.C. Lauterbur. Image formation by induced local interactions: examples employing nuclear magnetic resonance. *Nature*, 242:190–191, 1973.

[33] D. Le Bihan. Methods and applications of diffusion mri. In I.R. Young, editor, *Magnetic Resonance Imaging and Spectroscopy in Medicine and Biology.* John Wiley and Sons, 2000.

[34] N.K. Logothetis, J. Pauls, M. Augath, T. Trinath, and A. Oeltermann. Neurophysiological investigation of the basis of the fMRI signal. *Nature*, 412(6843):150–157, 2001.

[35] S. Mann and R. W. Picard. Virtual bellows: Constructing high quality stills from video. In *Proceedings of the International Conference on Image Processing*, pages 363–367, November 1994.

[36] M. Ng, R. Chan, T. Chan, and A. Yip. Cosine transform preconditioners for high resolution image reconstruction. *Linear Algebra Appls*, 316:89–104, 2000.

[37] M. Ng, R. Chan, and W. Tang. A fast algorithm for deblurring models with neumann boundary conditions. *SIAM Journal on Scientific Computing*, 21:851–866, 2000.

[38] N.X. Nguyen. *Numerical algorithms for image superresolution.* PhD thesis, Stanford University, Stanford, CA, 2000.

[39] M.F. Nitschke, A. Kleinschmidt, K. Wessel, and J. Frahm. Somatotopic motor representation in the human anterior cerebellum. a high-resolution functional mri study. *Brain*, 119:1023–1029, 1996.

[40] S. Ogawa, T.M. Lee, A.R. Kay, and D.W. Tank. Brain magnetic resonance imaging with contrast dependent on blood oxygenation. In *Proceedings of the National Academy of Sciences of the United States of America*, volume 87, pages 9868–9872, December 1990.

[41] S. Ogawa, D.W. Tank, R. Menon, J.M. Ellermann, S.G. Kim, H. Merkle, and K. Ugurbil. Intrinsic signal changes accompanying sensory stimulation: Functional brain mapping with magnetic resonance imaging. In *Proceedings of the National Academy of Sciences of the United States of America*, volume 89, pages 5951–5955, 1992.

[42] A. Papoulis. A new algorithm in spectral analysis and bandlimited extrapolation. *IEEE Trans. Cir. Sys.*, 22:735–742, 1975.

[43] G. Rees, K. Friston, and C. Koch. A direct quantitative relationship between the functional proporties of human and macaque V5. *Nature Neuroscience*, 3:716–723, 2001.

[44] K. Sauer and J. Allebach. Iterative reconstruction of band-limited images from nonuniformly spaced samples. *IEEE Trans. Circuits Syst,*, 34:1497–1505, 1987.

[45] R.R. Schultz and R.L. Stevenson. Extraction of high resolution frames from video sequences. *IEEE Transactions on Image Processing*, 5(6):996–1011, 1996.

[46] D. Slepian and H.O. Pollak. Prolate spheroidal wave functions, fourier analysis and uncertainty - I. *Bell System Tech. J.*, 40:43–63, 1961.

[47] H. Stark and P. Oskoui. High-resolution image recovery from image-plane arrays using convex projections. *J. Opt. Soc. Amer.*, 6:1715–1726, 1989.

[48] S. Sunaert, P. Van Hecke, G. Marchal, and G.A. Orban. Attention to speed of motion, speed discrimination, and task difficulty: an fmri study. In *Neuroimage*, volume 11, pages 612–623, 2000.

[49] A. Tekalp, M. Ozkan, and M. Sezan. High-resolution image reconstruction from lower-resolution image sequences and space varying image restoration. In *ICASSP*, volume 3, pages 169–172, San Fransisco, 1992.

[50] K.R. Thulborn, S.Y. Chang, G.X. Shen, and J.T. Voyvodic. High-resolution echo-planar fMRI of human visual cortex at 3.0 Tesla. *NMR Biomed*, 10(4–5):183–90, June 1997.

[51] R. Tsai and T. Huang. Multiframe image restoration and registration. In *Advances in Computer Vision and Image Processing*, volume 1, 1984.

[52] R. Turner and K. Friston. Functional mri. In *SPM Course*. Inst. of Neurology, Wellcome Dept. of Cognitive Neurology, 1997.

[53] R. Turner, A. Howseman, G.E. Rees, O. Josephs, and K. Friston. Functional magnetic resonance imaging of the human brain: data acquisition and analysis. *Experimental Brain Research*, 123(1–2):5–12, November 1998.

[54] H. Ur and D. Gross. Improved resolution from subpixel shifted pictures. *Computer Vision, Graphics, and Image Processing*, 54(2):181–186, 1992.

[55] C. Westbrook and C. Kaut. *MRI in practice*. Blackwell scientific publications, 1993.

Contents

Unité de recherche INRIA Sophia Antipolis
2004, route des Lucioles - BP 93 - 06902 Sophia Antipolis Cedex (France)

Unité de recherche INRIA Lorraine : LORIA, Technopôle de Nancy-Brabois - Campus scientifique
615, rue du Jardin Botanique - BP 101 - 54602 Villers-lès-Nancy Cedex (France)
Unité de recherche INRIA Rennes : IRISA, Campus universitaire de Beaulieu - 35042 Rennes Cedex (France)
Unité de recherche INRIA Rhône-Alpes : 655, avenue de l'Europe - 38330 Montbonnot-St-Martin (France)
Unité de recherche INRIA Rocquencourt : Domaine de Voluceau - Rocquencourt - BP 105 - 78153 Le Chesnay Cedex (France)

Éditeur
INRIA - Domaine de Voluceau - Rocquencourt, BP 105 - 78153 Le Chesnay Cedex (France)
http://www.inria.fr
ISSN 0249-6399